For the final published version see https://doi.org/10.1039/D2LC00028H

ARTICLE

Deciphering impedance cytometry signals with neural networks

Federica Caselli,*[a] Riccardo Reale,[b] Adele De Ninno,[c] Daniel Spencer,[d] Hywel Morgan [d] and Paolo Bisegna [a]

Received 00th January 20xx,
Accepted 00th January 20xx

DOI: 10.1039/x0xx00000x

Microfluidic impedance cytometry is a label-free technique for high-throughput single-cell analysis. Multi-frequency impedance measurements provide data that allows full characterization of cells, linking electrical phenotype to individual biophysical properties. To efficiently extract the information embedded in the electrical signals, potentially in real-time, tailored signal processing is needed. Artificial intelligence approaches provide a promising new direction. Here we demonstrate the ability of neural networks to decipher impedance cytometry signals in two challenging scenarios: (i) to determine the intrinsic dielectric properties of single cells directly from raw impedance data streams, (ii) to capture single-cell signals that are hidden in the measured signals for coincident cells. The accuracy of the results and the high processing speed (fractions of ms per cell) demonstrates that neural networks can have an important role in impedance-based single-cell analysis.

1 Introduction

The synergistic convergence of microfluidics and machine learning is expected to play a game-changing role in cell analysis and manipulation. Combining microfluidics - to acquire vast amounts of data at the single cell level - with machine learning - to analyse such complex data effectively - represents an emerging opportunity in biotechnology that remains largely untapped[1,2]. Machine learning potentially enables the development of *intelligent* microfluidic platforms operated by data-driven models and characterized by increased automation[3,4]. This offers advantages in high-throughput and precision analysis of cells. Human-based control and data analysis is a labour-intensive and time-consuming process, also prone to bias by the user and low accuracy. Real-time monitoring and automatic control are highly desirable to instruct normal operation as well as to ensure proper functioning in the case of abnormalities (e.g., unexpected clogs or air bubbles).

In recent years, the integration of machine learning with microfluidics has led to improved imaging flow cytometry and image-activated cell sorting technologies[5–8]. Technological advances improved the trade-off between speed and accuracy[9] with optimal machine learning approaches developed for single-cell data analysis. The techniques can be categorized into two groups based on the type of data that are analyzed by a trained model, namely raw images or features extracted from images[10]. Aspects to be considered include the need for large and representative training data sets with data normalization and augmentation; the need for labelled data in supervised learning approaches; the selection of tailored network architectures along with possible transfer learning strategies.

A research field that could benefit the developments of machine learning to cell analysis and sorting is single-cell impedance cytometry. This technique is a label-free and high-throughput method to characterize cellular systems based on their electrical phenotype[11–13]. Applications range from fundamental life-science and drug assessment research to point-of-care diagnostics and precision medicine. The development of novel approaches for multiparametric impedance-based characterization at high throughput requires tailored strategies for signal processing and data analysis.

In contrast to other microfluidic fields (especially imaging flow cytometry), the application of machine learning to impedance cytometry is relatively unexplored. Recent studies have considered the use of machine learning tools to classify biological cells based on electrical features[14–20] (*i.e.*, scalar parameters extracted from the raw impedance signals). For instance, Schutt *et al.*[14] used a *k*-means algorithm for subpopulation clustering of peripheral blood mononuclear cells, based on peak voltage and phase; Ahuja *et al.*[16] used a Support Vector Machine (SVM) classifier to discriminate between live and dead T47D breast cancer cells, using peak impedance magnitude and phase at four frequencies; D'Orazio *et al.*[17] used a SVM classifier in an 8-class pollen grain classification task, based on magnitude and phase at two frequencies; Yang *et al.*[18] used a backpropagation neural network to classify MCF-7 breast cancer cells with different deformability, using impedance magnitude and two transit time metrics; Feng *et al.*[20] used fully connected networks to estimate three biophysical parameters

[a] Department of Civil Engineering and Computer Science, University of Rome Tor Vergata, Rome, Italy. E-mail: caselli@ing.uniroma2.it
[b] Center for Life Nano Science@Sapienza, Italian Institute of Technology (IIT), Rome, Italy.
[c] Italian National Research Council - Institute for Photonics and Nanotechnologies (CNR - IFN), Rome, Italy.
[d] School of Electronics and Computing Science, and Institute for Life Sciences, University of Southampton, Highfield, Southampton, UK.
Electronic Supplementary Information (ESI) available. See DOI: 10.1039/x0xx00000x

from peak impedance amplitude at four frequencies to classify 5 cell types.

In contrast to these studies, we describe the use of machine learning to directly process time-domain raw impedance signals (instead of pre-extracted electrical features), an approach that is in its infancy. Wang and co-authors used Convolutional Neural Networks (CNN) to implement pattern recognition in possibly interfering signal waveforms from a Coulter sensor network[21], and implemented a closed-loop feedback control that drives a programmable pressure pump to maintain a desired cell flow speed[22]. Honrado *et al.*[23] developed a Recurrent Neural Network (RNN) to perform real-time feature extraction from single-cell impedance signals, demonstrating accurate characterization of size, velocity, and cross-sectional position of beads, red blood cells, and yeasts, with a unitary prediction time of 0.4 ms.

In this paper we demonstrate the use of tailored network architectures to tackle two challenging tasks in microfluidic impedance cytometry, namely, single-cell electrical phenotyping and coincidence resolution.

Single-cell electrical phenotyping refers to the characterization of the intrinsic electrical properties of single cells, that can aid in understanding biological processes including disease progression at the cellular and molecular levels[24]. Assuming a single-shell model[25], the electrical properties can be described in terms of the conductivity and permittivity of the membrane and cytoplasm, estimated by fitting the model to experimental impedance spectra. High speed multi-frequency impedance measurements have shown that impedance spectra of individual cells can be acquired at rates of up to a thousand cells per second[26]. Further developments such as active on-the-fly particle sorting[27] require high *processing* throughput (number of analysed single-particle signals per unit time). This calls for tailored signal-processing approaches that can implement a complete processing workflow - from event-detection in the data stream to dielectric properties estimation - in real time. Neural networks are ideal candidates, as the main computation during network prediction consists of parallel matrix multiplications, resulting in high-speed processing[28]. To the best of our knowledge, this is the first time that neural networks have been used to determine the intrinsic dielectric properties of single cells directly form raw impedance data.

Coincidence resolution describes the analysis of interfering signals that are generated by the passage of two or more cells roughly simultaneously through the sensing region (i.e., a coincidence). The shape of the overall measured signal depends on the number and the properties (size, dielectric properties, relative position, velocity) of the individual interfering cells[29,30]. This results in a plethora of possible signal shapes that can hardly be handled by standard processing approaches that assume a unique and well-defined signal shape (typically a Gaussian or a bipolar Gaussian pulse). As in Coulter-type devices, coincidence reduces number of cells that can be analysed and can lead to errors in the measured cell properties[31]. Restricting coincidence to typically below 10% imposes a limit on the sample concentration (typically below 10^6 cell/ml), at the expense of increased reagent volume and increased assay time. We demonstrate the application of innovative neural network-based approaches to overcome this limitation. In fact, neural networks can uncover single-cell signals that are hidden in the overall measured signal.

In this paper, studies of single-cell electrical phenotyping and coincidence resolution are separately presented, highlighting the innovative concepts and experimental outcomes. Guidelines for future studies are presented, emphasizing current challenges of this new research direction.

2 Single-cell electrical phenotyping

2.1 Experimental data

The microfluidic impedance cytometer consists of a microfluidic channel (40 μm wide and 30 μm high) with several micron-sized electrodes, as shown in Fig. 1A. When an AC voltage is applied to a set of electrodes, a flowing cell perturbs the electrical current which is measured differentially (one electrode pair followed by a second pair). The measured differential signal has a bipolar Gaussian shape, where the peak amplitude corresponds to the cell impedance at that frequency. Low frequency (< 1MHz) impedance measurements provide a direct measurement of (electrical) cell size; at intermediate frequencies (1-5 MHz), the cell membrane capacitance dominates the measured impedance spectrum; at higher frequencies (>20MHz), the electrical properties are dominated by the cell cytoplasm and finally the nucleus (if present) at very high frequencies (cf. section S1 of the Supplementary Material). In Ref.[26], eight frequencies were applied simultaneously in order to measure the complete spectrum of single cells. These frequencies were spaced logarithmically apart between 250kHz and 50MHz. In this work the experimental dataset is taken from Ref.[26]

The sample contained a mixture of red blood cells (RBCs) and ghosts suspended in phosphate buffered saline (PBS). The RBC is the simplest model cell, and its dielectric characterization is critical in many applications, such as malaria diagnosis[32], understanding sickle-cell disease[33], and blood storage monitoring[34]. RBCs were sphered in order to simplify the analysis. Ghost cells were also used since their membranes reseal to a spherical shape and entrap a “cytoplasm” with well-defined dielectric properties. In addition, reference beads (7 μm diameter) were used for signal normalization. The flow rate was set to 40 μl/min, while the sampling rate was 57.6 kHz. Full details are provided in Ref.[26]

2.2 Dataset augmentation

Neural network models learn to map inputs to outputs given a training dataset of examples. Data augmentation encompasses a suite of techniques that enhance the size and quality of training datasets such that better machine learning models can be built using them[35,36]. Data augmentation attempts to increase the generalization ability of trained models by reducing overfitting (which occurs when a model describes features that arise from noise or variance in the training data, rather than the

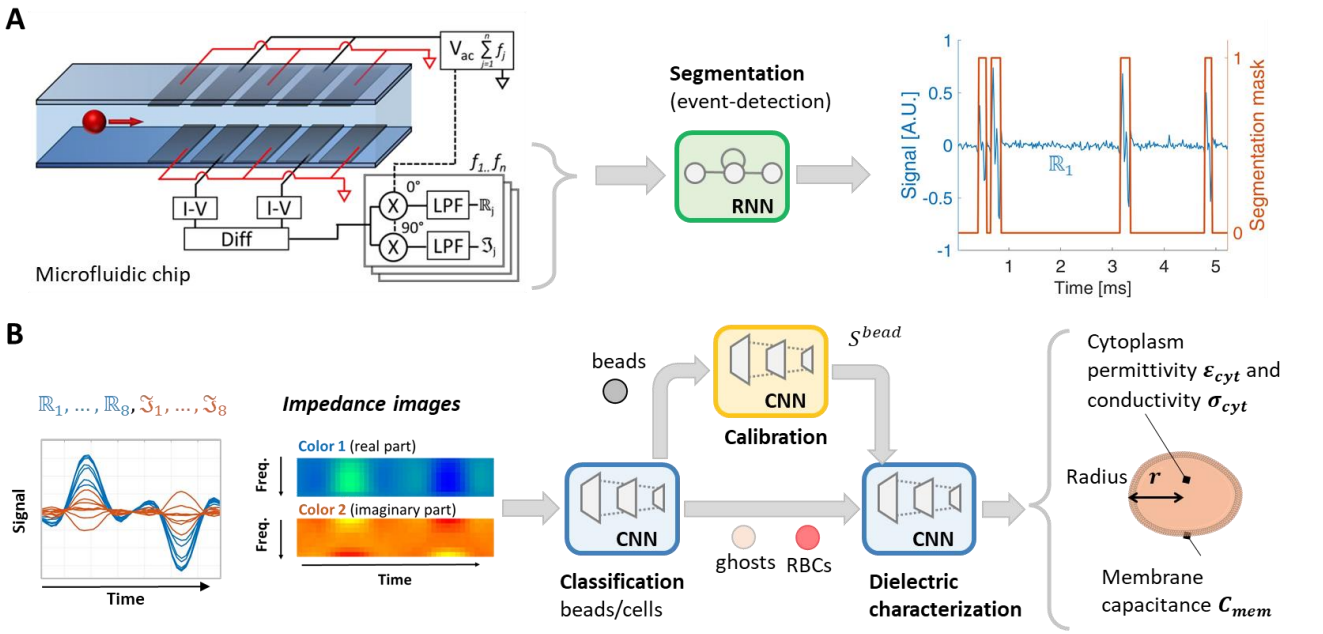

Fig. 1 Single-cell dielectric spectroscopy workflow. (A) An AC voltage signal containing n=8 frequencies is applied to two top electrodes of a microfluidic impedance chip, and the differential current is collected from the two opposite bottom electrodes. The signal is demodulated into its real ($\mathbb{R}_j$) and imaginary ($\mathfrak{I}_j$) components at each frequency f_j. The resulting 16 data streams are fed as inputs to a classification RNN that is trained to identify the data stream portions corresponding to individual flowing particles/cells (i.e., the network outputs a binary segmentation mask). (B) The signals $\mathbb{R}_j$ and $\mathfrak{I}_j$ of each detected particle/cell are reshaped as impedance images, which are fed into a classification CNN that performs particle classification (beads or cells). Cell impedance "images" are then processed by a regression CNN that predics cell size and dielectric properties, whereas bead signals are used to obtain the calibration signal S^{bead}. The image of the microfluidic chip in panel (A) is adapted with permission from Ref. 26.

underlying distribution from which the data were drawn[37]). The need for generalization is especially important for real-world data and can help networks overcome small datasets or datasets with imbalanced classes. While data augmentation is a common practice in image processing with neural networks, it is not established as a standard procedure for analysis of time series (like time-domain impedance signals). We implemented a data augmentation which mimics variations in the sample flow rate, and hence particle velocity. In particular, the original dataset was time-stretched and resampled to maintain the original sampling rate (Fig. S3 Supplementary Material). Five stretch values were considered, logarithmically spaced in the range 0.5-2.

In order to perform hold-out cross-validation, the augmented dataset was subdivided into training set, validation set, and test set according to the following proportions: 70%, 15%, 15%, respectively.

2.3 Neural network-based workflow

The overall signal-processing workflow (Fig. 1) is described below. Additional technical details are provided in section S3 of the Supplementary Material.

Segmentation of the raw data stream. The first step consists of identification of the data stream portions associated with cell passing through the sensing zone (i.e., data stream segmentation or event detection). To achieve this, we mimic a technique originally developed for Voice Activity Detection (VAD)[38]. Particle signals in the impedance data stream are considered as word sounds in an audio recording. The proposed approach is based on a Recurrent Neural Network (RNN) composed of five layers (Fig. S4 Supplementary Material): (i) sequence input layer, (ii) bidirectional Long Short Term Memory (bi-LSTM) layer, (iii) fully connected layer, (iv) softmax layer, (v) classification layer. The sequence input layer receives the impedance data stream, which is composed of 16 sequences (8 frequency channels, each with real and imaginary components). The final classification layer outputs a binary sequence wherein 0 indicates noise and 1 indicates particle-signal, thus yielding the data stream segmentation mask (Fig. 1A). The network was trained via supervised learning, by using a labelled dataset. The labelling (i.e., the target segmentation mask) was obtained by processing the data stream with a previously validated algorithm[39].

Cell dielectric characterization from impedance images. The single-cell signals, comprising 16 traces (8 frequencies, real and imaginary parts) are reshaped as *impedance images* (Fig. 1B), i.e. two-dimensional representations where the rows correspond to the different frequency channels and the columns correspond to the different time samples. Each image has two colours: one corresponds to the real signal component, and the other to the imaginary signal component. This novel concept of impedance image lends itself well to CNN-based processing. In particular, we used CNNs with the following architecture (Fig. S5 Supplementary Material): (i) image input layer, (ii) 3 repetitions of convolutional layer, batch normalization layer, and Rectifier Linear Unit (ReLU) layer, (iii) fully connected layer, (iv) depending on the network task (i.e., classification or

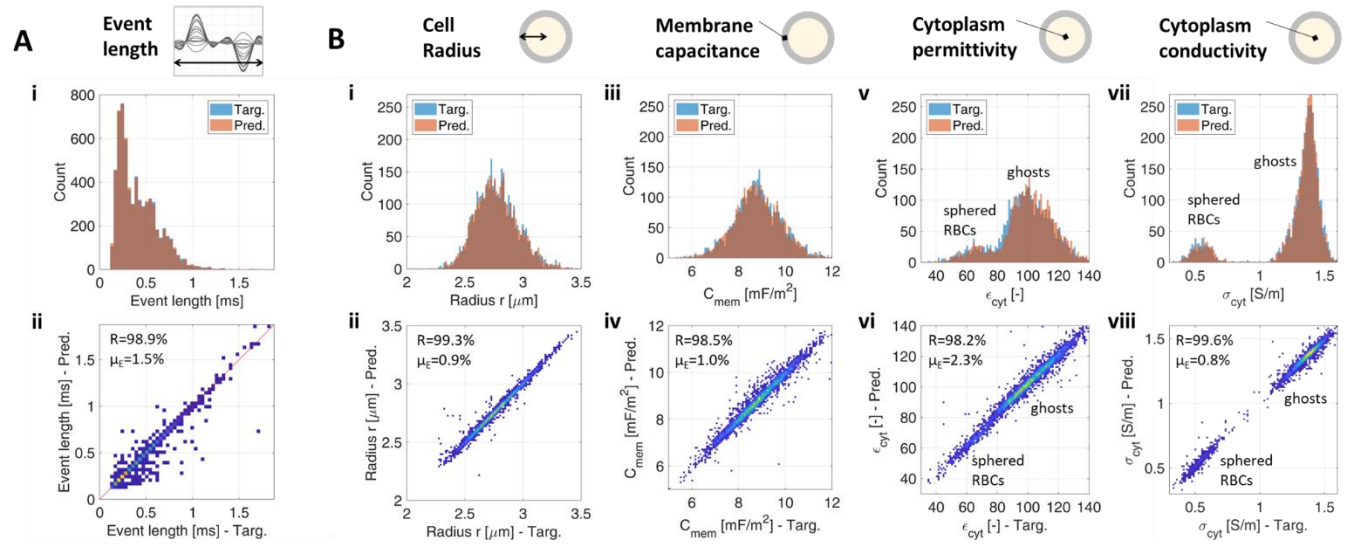

Fig. 2 Single-cell dielectric spectroscopy results (Targ: target; Pred: predicted). (A) Data streams segmentation: (i) histogram of predicted and target event length, (ii) density plot of predicted event length vs target event length. (B) Estimation of cell dielectric properties: histograms of predicted and target radius (i), membrane capacitance (iii), cytoplasm permittivity (v), and cytoplasm conductivity (vii), along with the associated density plots (ii), (iv), (vi), and (viii), respectively. Correlation coefficients R and average relative errors μ_E are also reported within the density plots.

regression), either a softmax layer followed by a classification layer, or a regression layer.

As detailed in Ref.[26], the measured frequency-dependent impedance for a single cell includes effects from the measurement hardware (non-linear behaviour of the electronics and chip parasitics), which need to be compensated. Therefore the measured cell impedance is normalized against the bead impedance (cf. section S1 Supplementary Material). This task is performed by a classification CNN which classifies the event impedance images in two classes (bead or cell), followed by a regression CNN which outputs the peak amplitudes of the bead signals, to be used for normalization.

The normalized cell impedance images are processed by a regression CNN that predicts the cell size (radius $\boldsymbol{r}$) and the cell intrinsic dielectric properties, namely, membrane capacitance $\boldsymbol{C_{mem}}$, cytoplasm conductivity $\boldsymbol{\sigma_{cyt}}$, and cytoplasm permittivity $\boldsymbol{\varepsilon_{cyt}}$.

The networks were trained via supervised learning, by using a labelled dataset. The labels (target class, target peak amplitudes, and target values of radius and dielectric properties) were obtained using standard signal processing algorithms based on template-fitting and impedance spectra fitting[11,26] (Fig. S2 Supplementary Material). Target features were scaled to the range [0, 1]. Neural network predictions were then scaled back to their original ranges.

2.4 Results

The results relevant to the segmentation of the data stream are shown in Table 1 and Fig. 2A. Table 1 shows the particle counting performance and summarises the number of correctly detected particles (true positives, TP), missed particles (false negatives, FN), noise regions misinterpreted as particles (false positives, FP), and the resulting values of sensitivity (S) and positive predictive value (PPV):

$$\mathrm{S} = \frac{\mathrm{TP}}{\mathrm{TP} + \mathrm{FN}}, \quad \mathrm{PPV} = \frac{\mathrm{TP}}{\mathrm{TP} + \mathrm{FP}}.$$

Fig. 2A evaluates the quality of event-length predictions. In particular, the histograms of predicted and target event length, and the density plot of predicted length against target length are shown in sub-panels (i) and (ii), respectively. The correlation coefficient (R) and the average relative error (μ_E) are 98.9% and 1.5%, respectively.

The results of system normalization using calibration beads are reported in Fig. S7, Supplementary Material. The accuracy of the binary classification of beads or cells is close to 100%, with unitary prediction time UT=0.10 ms. The latter is defined as the overall network prediction time divided by the cardinality of the test set. The relative error on the estimated bead calibration signal is lower than 3% (with UT=0.04 ms).

Fig. 2B shows results of cell dielectric characterization. In particular, the predicted values of cell radius and cell intrinsic properties (membrane capacitance, cytoplasm conductivity, and cytoplasm permittivity) are compared with target values using superimposed histograms and 2D density plots. Correlation coefficients (R) and average relative errors (μ_E) are also reported, highlighting the remarkable prediction capabilities of the network, which exhibited a unitary prediction time UT=0.11 ms.

As expected, RBCs and ghosts have similar radii and membrane capacitance (Fig. 2B, sub-panels (i)-(iv)), but different cytoplasm conductivity and permittivity (Fig. 2B, sub-panels (v)-(viii); Fig. S6, Supplementary Material). Whilst cytoplasm conductivity would be sufficient to distinguish RBCs and ghosts, the full set of properties could be useful for identifying subpopulations with similar electrical phenotype. For example, Honrado et al.[32]

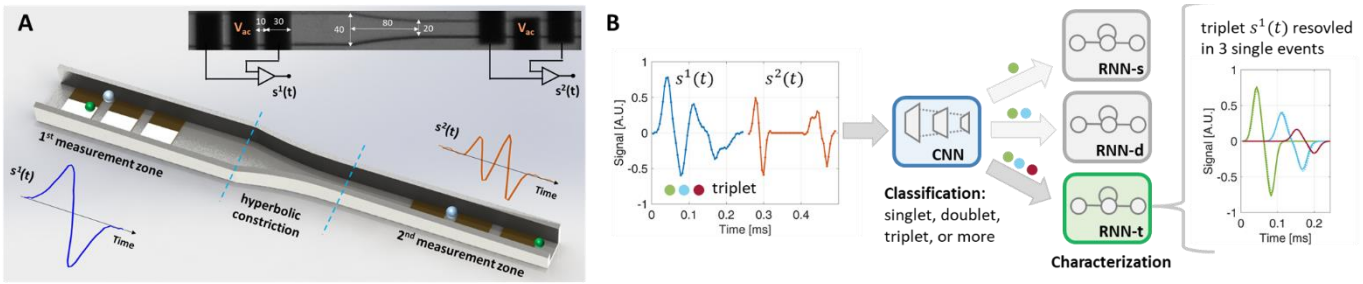

Fig. 3 Coincidence resolution workflow. (A) A microfluidic chip with two measurement zones separated by a hyperbolic constriction is used to acquire two electrical snapshots, $s^1(t)$ and $s^2(t)$ of each cluster of flowing particles (i.e. a single particle or a group of particles producing interfering signals). As shown in the inset, in each measurement zone three coplanar electrodes are used: AC voltage is applied to the central electrode and the differential current from the lateral electrodes is collected (indicated dimensions are in µm). (B) The signals $s^1(t)$ and $s^2(t)$ of each cluster are processed by a classification CNN that predicts the number of composing particles (i.e. it establishes if the cluster is a singlet, a doublet, a triplet, or a *k*-particle event with k>3). Depending on the number of composing particles, a suitable regression RNN is used to predict the features of the single-particle signals (RNN-s for singlets, RNN-d for doublets, RNN-t for triplets). In the example, a triplet is considered, and therefore RNN-t is used to unveil the three single-events embedded in $s^1(t)$. The picture of the microfluidic chip in panel (A) is adapted with permission from Ref. 30.

showed that the membrane capacitance and cytoplasmic conductivity of *Plasmodium falciparum*-infected RBCs increased with time, due to membrane alterations caused by parasite infection. Alterations of dielectric properties of RBCs have been related to oxygen carrying capacity[40], glucose homeostasis[41], and age[42]. Recently, the use of RBCs as multimodal standard particles with systematically modulated membrane capacitance and cytoplasm conductivity has been presented[43]. Machine learning could provide improved, high speed method for classifying these subtle differences between cells.

Table 1 Particle counting results

TP	FN	FP	S (%)	PPV (%)
6483	142	274	97.8	95.9

3 Coincidence resolution

This section introduces an original neural network-based approach to coincidence resolution.

3.1 Experimental data

The microfluidic cytometer in this case comprises two measurement zones separated by a hyperbolic constriction (Fig. 3A). The microchannel is 40 µm wide in the first measurement zone and 20 µm wide in the second one, while channel height is 20 µm. Each measurement zone has three coplanar electrodes: AC voltage is applied to the central electrode and the differential current from the lateral electrodes is measured. Each particle contributes to the measured signal giving a bipolar Gaussian signal (one for each sensing zone). However, when two or more particles flow in close proximity their signals interfere, and the overall measured signal is given by the superposition of the individual bipolar Gaussian profiles (see example in Fig. S8, Supplementary Material). Since the relative position of particles changes with time because they generally have different velocities, signals generated by more than one particle (i.e. coincidences) will have different shapes in the two measurement zones. Therefore, the electrical signals from two measurement zones instead of one, provide valuable information for coincidence resolution[30].

The experimental dataset used for this case study is taken from Ref.[30] The samples contained either beads (6 µm diameter) or red blood cells suspended in PBS. Since the application was focused on coincidence resolution (rather than dielectric characterization), only one frequency was used in each measurement zone, and only the real component of the measured signals was recorded. The flow rate was set to 30 µl/min, while the sampling rate was 230 kHz. Full details are provided in Ref.[30]

3.2 Generation of synthetic multi-particle signals and data augmentation

Since the issue of coincidence resolution is especially challenging, we designed a strategy to build artificial *k*-particle events (i.e. coincidence signals generated by *k* particles with known properties). As shown in Fig. S9A-B, Supplementary Material, single-particle signals were extracted from an experimental data stream of beads/RBCs at low concentration (10^5 particles per ml); synthetic *k*-particle events were obtained by randomly superimposing single-particle signals extracted from the available pool. In order to mimic an experimental dataset with extreme conditions (very high coincidence), a concentration of 10^7 particles per ml was used, assuming a Poisson distribution for particle arrival times. For these conditions, the expected fraction of singlets, doublets and triplets is 52%, 25%, and 12%, respectively[30]. The overall fraction of *k*-particle events with *k*>3 is 11% (of which: 5.6% with *k*=4, 2.8% with *k*=5, 1.4% with *k*=6, and progressively lower fractions for higher values of *k*).

To achieve robust network training, reduce the risk of overfitting and increase the network generalization capabilities, we implemented a two-fold data augmentation strategy. This is based on (i) amplitude augmentation at the level of the extracted single-particle signals (before their superposition), and (ii) velocity augmentation at the level of the assembled *k*-particle signals. Each extracted single-particle signal produced four additional single-particle signals (Fig. S9C-D, Supplementary Material). The logarithm of the amplitude

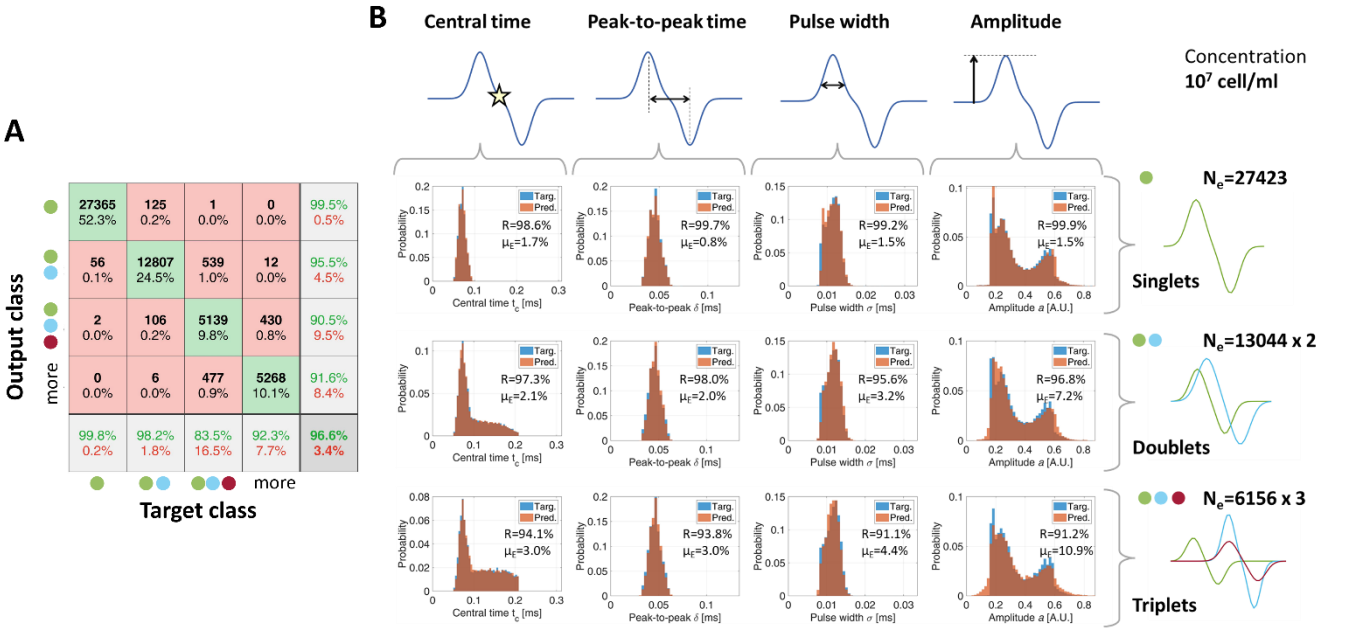

Fig. 4 Coincidence resolution results. (A) Confusion matrix of coincidence classification into singlet, doublet, triplet or more (i.e., *k*-particle event with *k*>3). Normalizations by row (i.e., precision) and by column (i.e., recall) are also reported. (B) Histograms of target and predicted features (i.e., central time, peak-to-peak time, pulse width, and amplitude) of the composing single-particle signals (Targ: target; Pred: predicted). The collection of features of single-particle signals composing singlets, doublets, and triplets are plotted on separate rows (from top to bottom).

amplification factor was randomly uniformly distributed in the range 0.25-4. Each assembled *k*-particle signal produced four additional *k*-particle signals (Fig. S10, Supplementary Material). The logarithm of the stretch factor was randomly uniformly distributed in the range 0.5-2. More than 533k synthetic multi-particle signals (285k singlets, 133k doublets, 61k triplets, and 54k clusters involving more than 3 particles) were build and used to train the networks.

The test dataset was generated with a concentration of 10^7 particles per ml following the same procedure (without data augmentation), by superposing single-bead signals and single-RBC signals extracted from two data streams at low concentration (2 x 10^5 particles per ml). As recommended to assess network generalization capability, these were new data streams (i.e., not the same set as used in training).

3.3 Neural network-based workflow

In this section the architecture of the signal-processing workflow (Fig. 3B) is described. Additional technical details are provided in Section S7 of the Supplementary Material.

Classification. The first task is classification of *k*-particle signals based on the number of measured particles, i.e. singlets (*k*=1), doublets (*k*=2), triplets (*k*=3), and more (*k*≥4). This task is performed by a CNN with the same main structure as that used for single-cell dielectric characterization (Fig. S11, Supplementary Material). As illustrated in Fig. 3B, the network receives as an input the two electrical signals for the event (one from each measurement zone) and predicts as an output the corresponding class (singlet, doublet, triplet, or more).

Regression. Events classified as singlets, doublets, or triplets are fed as input to regression RNNs that are trained to predict the features of the individual bipolar signals that compose a singlet, doublet, or triplet, respectively. In particular, each individual bipolar signal is characterized by four features (Fig. S12, Supplementary Material): the central time $\boldsymbol{t_c}$, the peal-to-peak time $\boldsymbol{\delta}$, the pulse width $\boldsymbol{\sigma}$, and the signal peak amplitude $\boldsymbol{a}$. The RNNs have the same main architecture (Fig. S12, Supplementary Material) as that used for data stream segmentation. Target features were obtained using standard template fitting performed on the individual bipolar signal (before their superposition), and were scaled to the range [0, 1]. Neural network predictions were then scaled back to their original ranges.

3.4 Results

The results of particle counting are shown in Fig. 4A. On the confusion matrix plot, the rows correspond to the predicted class (Output Class) and the columns correspond to the true class (Target Class). The diagonal cells correspond to observations that are correctly classified. The off-diagonal cells correspond to incorrectly classified observations. Both the number of observations and the percentage of the total number of observations are shown in each cell. More than 52k events were considered. An overall accuracy of 97% is achieved and all classes have precision higher than 90%. Full precision and recall are achieved on singlets, whereas precision and recall on doublets are 95% and 98%, respectively. Unitary prediction time was UT=0.05 ms.

The results of single-particle signal characterization are shown in Fig. 4B, which shows (column-by-column) the histograms of target and predicted features, namely, central time (with respect to the cluster start sample), peak-to-peak time, pulse

width, and signal amplitude. The features of the individual events composing singlets, doublets, and triplets are plotted in separate histograms (row-by-row). As expected, the histograms of peak-to-peak time, pulse width, and amplitude of the individual events exhibit the same distribution irrespective of the cluster they come from (singlet, doublet, or triplet). On the other hand, for the histogram of central time a tail of events at higher values appears for doublets and triplets, representing the second and – for the triplets - third events of the cluster. Correlation coefficients (R) and average relative errors (μ_E) are also reported within the histograms, showing the good prediction capabilities of the networks. All features have μ_E lower than 4%, except for the amplitudes of events from doublets or triplets (μ_E of 7% and 11%, respectively). Density plots of target and predicted features are shown in Fig. S13, Supplementary Material. Unitary predictions times of the RNN used for singlets, doublets, and triplets were 0.69 ms, 0.82 ms, and 0.86 ms, respectively.

4 Discussion & outlook

The results presented in this work demonstrate the ability of neural networks to decipher at high speed the information embedded in raw impedance data streams, in challenging scenarios involving multi-frequency analysis or intricate signals. From an application point of view, we developed an approach to single-cell dielectric spectroscopy that combines high-throughput acquisition with high-throughput processing and is therefore compatible with real-time sorting. Also, we demonstrate the feasibility of the approach in overcoming the limitation of sample concentration by resolving coincident events. This is valuable in applications demanding accurate counting where high sample dilution is not possible.

In developing our methods, two network types were considered: recurrent neural networks, which are frequently used to process data with a temporal dimension, and convolutional neural networks, which are widely used in image analysis. After preliminary investigation, for each task the network exhibiting best performances was chosen. Extensive comparison with fine optimization of all network hyperparameters is outside the scope of this paper. A Matlab implementation on a PC resulted in unitary prediction times of fractions of ms. Faster processing could be achieved with dedicated hardware solutions.

Data augmentation was used to increase the generalization capability of the networks. We considered augmentation at the level of signal amplitude, to mimic a broad range of particle sizes, and augmentation at the level of time domain, to mimic e.g., variations in particle velocity arising from flow-rate changes. Other approaches to data augmentation could be devised (e.g. translation in time, noise addition) and finite element simulated signals could also play a role in network training (e.g. network weights initialization).

A challenging issue is the need for a ground truth providing labels. In this work we used either reference non-real-time algorithms, or suitably built synthetic signals. However, other applications may profit from the development of semi-supervised or unsupervised learning approaches tailored to impedance cytometry signals.

In this work, neural networks are trained to predict single-cell features. These features can be used as input to classifier models (e.g., Support Vector Machines) trained to discriminate cell phenotypes via supervised learning. Alternatively, a classification neural network could be trained to directly predict the cell phenotype from raw impedance signals. In that case, the network itself would identify the most distinctive features that may be hidden in the input signal, which could lead to increased classification accuracy (although the physical meaning of the network-selected features may be not obvious). Furthermore, unsupervised learning approaches (e.g., based on Generative Adversarial Networks[44]) might lead to the identification of unknown cell types.

Artificial Intelligence (AI) is now pervasive in image processing. The use of AI to analyse impedance signals, as described in this work, could foster the synergistic integration of impedance flow cytometry and imaging flow cytometry. Universal networks for impedance cytometry could be developed, analogous to AlexNet or GoogleNet for image processing. To this end, raw impedance data streams could be collected across different laboratories, to increase network generalization capabilities.

The synergistic convergence of microfluidics and machine learning is opening new challenges and opportunities for next generation impedance cytometry systems.

Author Contributions

Federica Caselli: Conceptualization, Methodology, Software, Formal analysis, Resources, Writing - Original Draft, Supervision, Project administration, Funding acquisition. **Riccardo Reale:** Investigation, Data Curation. **Adele De Ninno:** Investigation, Funding acquisition. **Daniel Spencer:** Investigation, Data Curation. **Hywel Morgan:** Conceptualization, Resources, Writing – review & editing. **Paolo Bisegna:** Conceptualization, Methodology, Software, Writing – review & editing.

Conflicts of interest

There are no conflicts to declare.

Acknowledgements

This work was supported by Regione Lazio under grant E85F21002390002 (MicroSystemQ project, Research Groups 2020 Programme).

References

1 J. Riordon, D. Sovilj, S. Sanner, D. Sinton and E. W. K. Young, *Trends Biotechnol.*, 2019, **37**, 310–324.

2 A. Isozaki, J. Harmon, Y. Zhou, S. Li, Y. Nakagawa, M. Hayashi, H. Mikami, C. Lei and K. Goda, *Lab Chip*, 2020, 20, 3074–3090.

3 E. A. Galan, H. Zhao, X. Wang, Q. Dai, W. T. S. Huck and S.

Ma, *Matter*, 2020, 3, 1893–1922.
4 J. Zheng, T. Cole, Y. Zhang, J. Kim and S.-Y. Tang, *Biosens. Bioelectron.*, 2021, **194**, 113666.
5 Y. Han, Y. Gu, A. C. Zhang and Y. H. Lo, *Lab Chip*, 2016, 16, 4639–4647.
6 S. Luo, Y. Shi, L. K. Chin, P. E. Hutchinson, Y. Zhang, G. Chierchia, H. Talbot, X. Jiang, T. Bourouina and A.-Q. Liu, *Adv. Intell. Syst.*, 2021, 2100073.
7 D. M. D. Siu, K. C. M. Lee, M. C. K. Lo, S. V. Stassen, M. Wang, I. Z. Q. Zhang, H. K. H. So, G. C. F. Chan, K. S. E. Cheah, K. K. Y. Wong, M. K. Y. Hsin, J. C. M. Ho and K. K. Tsia, *Lab Chip*, 2020, **20**, 3696–3708.
8 A. Isozaki, H. Mikami, H. Tezuka, H. Matsumura, K. Huang, M. Akamine, K. Hiramatsu, T. Iino, T. Ito, H. Karakawa, Y. Kasai, Y. Li, Y. Nakagawa, S. Ohnuki, T. Ota, Y. Qian, S. Sakuma, T. Sekiya, Y. Shirasaki, N. Suzuki, E. Tayyabi, T. Wakamiya, M. Xu, M. Yamagishi, H. Yan, Q. Yu, S. Yan, D. Yuan, W. Zhang, Y. Zhao, F. Arai, R. E. Campbell, C. Danelon, D. Di Carlo, K. Hiraki, Y. Hoshino, Y. Hosokawa, M. Inaba, A. Nakagawa, Y. Ohya, M. Oikawa, S. Uemura, Y. Ozeki, T. Sugimura, N. Nitta and K. Goda, *Lab Chip*, 2020, **20**, 2263–2273.
9 A. Isozaki, H. Mikami, K. Hiramatsu, S. Sakuma, Y. Kasai, T. Iino, T. Yamano, A. Yasumoto, Y. Oguchi, N. Suzuki, Y. Shirasaki, T. Endo, T. Ito, K. Hiraki, M. Yamada, S. Matsusaka, T. Hayakawa, H. Fukuzawa, Y. Yatomi, F. Arai, D. Di Carlo, A. Nakagawa, Y. Hoshino, Y. Hosokawa, S. Uemura, T. Sugimura, Y. Ozeki, N. Nitta and K. Goda, *Nat. Protoc.*, 2019, **14**, 2370–2415.
10 S. Ota, I. Sato and R. Horisaki, *Microscopy*, 2020, **69**, 61–68.
11 C. Honrado, P. Bisegna, N. S. Swami and F. Caselli, *Lab Chip*, 2021, **21**, 22–54.
12 H. Daguerre, M. Solsona, J. Cottet, M. Gauthier, P. Renaud and A. Bolopion, *Lab Chip*, 2020, **20**, 3665–3689.
13 F. Gökçe, P. S. Ravaynia, M. M. Modena and A. Hierlemann, *Biomicrofluidics*, , DOI:10.1063/5.0073457.
14 J. Schütt, D. I. Sandoval Bojorquez, E. Avitabile, E. S. Oliveros Mata, G. Milyukov, J. Colditz, L. G. Delogu, M. Rauner, A. Feldmann, S. Koristka, J. M. Middeke, K. Sockel, J. Fassbender, M. Bachmann, M. Bornhäuser, G. Cuniberti and L. Baraban, *Nano Lett.*, 2020, **20**, 6572–6581.
15 J. Sui, P. Xie, Z. Lin and M. Javanmard, *Talanta*, 2020, **215**, 120791.
16 K. Ahuja, G. M. Rather, Z. Lin, J. Sui, P. Xie, T. Le, J. R. Bertino and M. Javanmard, *Microsystems Nanoeng.*, 2019, **5**, 34.
17 M. D'Orazio, R. Reale, A. De Ninno, M. A. Brighetti, D. A. Mencattini, L. Businaro, E. Martinelli, P. Bisegna, A. Travaglini and F. Caselli, *IEEE Trans. Biomed. Eng.*, , DOI:10.1109/TBME.2021.3109384.
18 D. Yang, Y. Zhou, Y. Zhou, J. Han and Y. Ai, *Biosens. Bioelectron.*, 2019, **133**, 16–23.
19 Y. Zhao, K. Wang, D. Chen, B. Fan, Y. Xu, Y. Ye, J. Wang, J. Chen and C. Huang, *Biosens. Bioelectron.*, 2018, **111**, 138–143.
20 Y. Feng, Z. Cheng, H. Chai, W. He, L. Huang and W. Wang, *Lab Chip*, 2021.
21 N. Wang, R. Liu, N. Asmare, C. H. Chu and A. F. Sarioglu, *Lab Chip*, 2019, **19**, 3292–3304.
22 N. Wang, R. Liu, N. Asmare, C.-H. Chu, O. Civelekoglu and A. F. Sarioglu, *Lab Chip*, 2021, **21**, 1916–1928.
23 C. Honrado, J. S. McGrath, R. Reale, P. Bisegna, N. S. Swami and F. Caselli, *Anal. Bioanal. Chem.*, 2020, **412**, 3835–3845.
24 M. A. Mansor and M. R. Ahmad, *Int. J. Mol. Sci.*, 2015, **16**, 12686–12712.
25 H. Pauly and H. P. Schwan, *Z. Naturforsch. B*, 1959, **14**, 125–131.
26 D. Spencer and H. Morgan, *ACS Sensors*, 2020, **5**, 423–430.
27 B. de Wagenaar, S. Dekker, H. L. de Boer, J. G. Bomer, W. Olthuis, A. Van Den Berg and L. I. Segerink, *Lab Chip*, 2016, **16**, 1514–1522.
28 P. Eulenberg, N. Köhler, T. Blasi, A. Filby, A. E. Carpenter, P. Rees, F. J. Theis and F. A. Wolf, *Nat. Commun.*, 2017, **8**, 1–6.
29 U. Hassan and R. Bashir, *Lab Chip*, 2014, **14**, 4370–4381.
30 F. Caselli, A. De Ninno, R. Reale, L. Businaro and P. Bisegna, *IEEE Trans Biomed Eng*, 2020, **68**, 340–349.
31 E. J. W. Wynn and M. J. Hounslow, *Powder Technol.*, 1997, **93**, 163–175.
32 C. Honrado, L. Ciuffreda, D. Spencer, L. Ranford-Cartwright and H. Morgan, *J. R. Soc. Interface*, 2018, **15**, 20180416.
33 J. Liu, Y. Qiang and E. Du, *Electrophoresis*, 2021, **42**, 667–675.
34 S. W. Herenda, C. S. Widodo, D. R. Santoso and W. Sugianto, in *AIP Conference Proceedings*, 2020, vol. 2314.
35 C. Shorten and T. M. Khoshgoftaar, *J. Big Data*, 2019, **6**, 60.
36 B. K. Iwana and S. Uchida, *PLoS One*, 2021, 16, e0254841.
37 G. I. Webb, in *Encyclopedia of Machine Learning*, eds. C. Sammut and G. I. Webb, Springer US, Boston, MA, 2010, p. 744.
38 F. Eyben, F. Weninger, S. Squartini and B. Schuller, in *ICASSP, IEEE International Conference on Acoustics, Speech and Signal Processing - Proceedings*, 2013, pp. 483–487.
39 F. Caselli and P. Bisegna, *IEEE Trans Biomed Eng*, 2016, **63**, 415–422.
40 J. Liu, Y. Qiang, O. Alvarez and E. Du, *ACS Sensors*, 2019, **4**, 1783–1790.
41 E. Levy, G. Barshtein, L. Livshits, P. Ben Ishai and Y. Feldman, *J. Phys. Chem. B*, 2016, **120**, 10214–10220.
42 Z. Gagnon, J. Gordon, S. Sengupta and H. C. Chang, *Electrophoresis*, 2008, **29**, 2272–2279.
43 A. Salahi, C. Honrado, A. Rane, F. Caselli and N. S. Swami, *Anal. Chem.*, 2022, **94**, 2865–2872.
44 I. J. Goodfellow, J. Pouget-Abadie, M. Mirza, B. Xu, D. Warde-Farley, S. Ozair, A. Courville and Y. Bengio, in *Advances in Neural Information Processing Systems*, 2014, vol. 3.

